Check for updates

Magnetically responsive polycaprolactone nanocarriers for application in the biomedical field: magnetic hyperthermia, magnetic resonance imaging, and magnetic drug delivery†

Marta Szczęch, [a] Davide Orsi, [b] Natalia Łopuszyńska,[c] Luigi Cristofolini, [b]
Krzysztof Jasiński, [c] Władysław P. Węglarz, [c] Franca Albertini,[d] Sami Kereïche[e]
and Krzysztof Szczepanowicz [*a]

There are huge demands on multifunctional nanocarriers to be used in nanomedicine. Herein, we present a simple and efficient method for the preparation of multifunctional magnetically responsive polymeric-based nanocarriers optimized for biomedical applications. The hybrid delivery system is composed of drug-loaded polymer nanoparticles (poly(caprolactone), PCL) coated with a multilayer shell of polyglutamic acid (PGA) and superparamagnetic iron oxide nanoparticles (SPIONs), which are known as bio-acceptable components. The PCL nanocarriers with a model anticancer drug (Paclitaxel, PTX) were formed by the spontaneous emulsification solvent evaporation (SESE) method, while the magnetically responsive multilayer shell was formed *via* the layer-by-layer (LbL) method. As a result, we obtained magnetically responsive polycaprolactone nanocarriers (MN-PCL NCs) with an average size of about 120 nm. Using the 9.4 T preclinical magnetic resonance imaging (MRI) scanner we confirmed, that obtained MN-PCL NCs can be successfully used as a MRI-detectable drug delivery system. The magnetic hyperthermia effect of the MN-PCL NCs was demonstrated by applying a 25 mT radio-frequency (f = 429 kHz) alternating magnetic field. We found a Specific Absorption Rate (SAR) of 55 W g^{-1}. The conducted research fulfills the first step of investigation for biomedical application, which is mandatory for the planning of any *in vitro* and *in vivo* studies.

1. Introduction

The blurring of the boundaries between chemistry, physics, material science, and biology has revolutionized medicine. Recent advances in domains such as nanotechnology and materials science have added many new tools for studying biological mechanisms and added many weapons for the treatment of disease.[1] The most spectacular example is the development of nanoparticles, *i.e.*, particles in size below a few hundreds of nanometers. The nanometer is a functional scale

ªJerzy Haber Institute of Catalysis and Surface Chemistry, Polish Academy of Sciences, Krakow, Poland. E-mail: ncszczep@cyf-kr.edu.pl; Fax: +48-124251923; Tel: +48-126395121

ᵇDepartment of Mathematical, Physical and Computer Sciences, University of Parma, Parma, Italy

ᶜHenryk Niewodniczański Institute of Nuclear Physics, Polish Academy of Sciences, Krakow, Poland

ᵈInstitute of Materials for Electronics and Magnetism, National Research Council (CNR), Parma, Italy

ᵉInstitute of Biology and Medical Genetics, First Faculty of Medicine, Charles University, Prague, Czech Republic

† Electronic supplementary information (ESI) available. See DOI: 10.1039/d0ra07507h

in biology, for example, proteins are natural nanomaterials that play essential roles in living organisms, *e.g.*, cellular communication and motility. Magnetic nanoparticles have been used in biomedicine for a variety of applications such as cell sorting and tracking, drug delivery, sensing, and imaging.[1–6] Among them, superparamagnetic iron oxide nanoparticles (SPIONs), which are particles formed by small crystals of iron oxide (commonly magnetite, Fe_3O_4, or maghemite, Fe_2O_3), have been widely utilized due to unique nanoscale physicochemical properties, *e.g.* biocompatibility.[6–12] Other metals such as cobalt and nickel are highly magnetic but also toxic, limiting their use in biomedical applications.[8,13,14] The unique properties of SPIONs offer a high potential for several biomedical applications, such as cellular therapy, cell labeling or targeting, as a tool for cell-biology research to separate and purify cell populations, tissue repair, drug delivery, magnetic resonance imaging (MRI), hyperthermia, magnetofection; *etc.*[1,7,11,12,15,16] In most of the applications, the SPIONs perform best when their size is in the range of 6–15 nm.[7,9,17] Magnetite and maghemite nanoparticles of this size show a superparamagnetic behaviour, *i.e.*, they become magnetized up to their saturation magnetization under the application of an external magnetic field, and

they no longer exhibit any residual magnetic interaction (no magnetic remanence) when the magnetic field is removed. Particles in that size range are rapidly removed through extravasations and renal clearance.[7] However, 'naked' nanoparticles are unstable over a longer period, they tend to form agglomerates, they are chemically highly active, and are easily oxidized in air, resulting generally in loss of magnetism and dispersibility.[1,4,9,10,18] Therefore, the bio-medical application associated with the use of SPIONs requires their surface modification that may involve coating with organic species such as surfactants, polymers or proteins, or coating with an inorganic layer, such as silica, gold or carbon.[8–10,19] It is noteworthy that in many cases such modification not only stabilizes the SPIONs but can also be used for further functionalization depending on the desired application. Encapsulation into polymeric nanoparticles or other nanocarriers is one of the promising approaches to overcome weaknesses mentioned above. Moreover, formed magnetically responsive nanocarriers can be easily optimized/functionalized for biomedical application, e.g., size can be optimized for passive drug delivery based on the EPR effect (diameter below 200 nm).[20,21] To achieved this, several strategies for the preparation of magnetically responsive nanoparticles/nanocarriers have been proposed. They include the following systems: polymeric nanoparticles, liposomes, polymeric micelles, polymerosomes as well as core/shell nanoparticles.[22–33] Particularly, polymeric nanocarriers formed with biocompatible, biodegradable, and bioacceptable components provide numerous advantages including long-term stability, a high loading capacity of hydrophobic drugs, and versatilities of surface modification.[34] The most interesting and powerful method of surface modification is the sequential adsorption of charged nano-objects called the layer-by-layer method (LbL).[35–37] The advantages of the LbL method are its ease of manipulation and the multifunctionality that comes from the possibility of modification of the multilayer shell by functional species e.g., antibodies, aptamers, and inorganic nanoparticles, including SPIONs.[37–45]

In this work, we report a simple and efficient method of the formation of multifunctional magnetically responsive polymeric nanocarriers optimized for biomedical applications. Polymeric nanocarriers composed with poly(caprolactone) (PCL) were prepared by the spontaneous emulsification solvent evaporation (SESE) method.[46] The model anticancer drug (Paclitaxel, PTX) was encapsulated into PCL NCs, and such formed nanocarriers were further functionalized by the layer-by-layer method. Magnetic nanoparticles together with polyglutamic acid (PGA) were used as charged nano-objects for multilayer shell formation. The developed magnetically responsive polycaprolactone nanocarriers (MN-PCL NCs) were characterized, their properties were optimized for a combination of passive and magnetic drug delivery that can be monitored by MRI, and finally, their capability to locally increase temperature under radio-frequency alternating magnetic fields (local magnetic hyperthermia) was demonstrated. For better understanding and tracking presented research, the list of abbreviations of tested samples are presented in Table 1.

Table 1 Abbreviations of tested samples

Abbreviation	Meaning
MN-PCL NCs	Magnetically responsive polycaprolactone nanocarriers
PCL NCs	Poly(caprolactone) nanocarriers

2. Materials and methods

2.1 Chemicals

Superparamagnetic iron oxide nanoparticles (SPIONs) with the size 8 ± 3 nm were purchased from PlasmaChem, Berlin, Germany. Polymers : polycaprolactone (PCL average $M_w \sim 14\,000$), poly-L-lysine hydrobromide (PLL average M_w 15 000 to 30 000), poly-L-glutamic acid sodium salt (PGA average M_w 5000 to 50 000), poly(allylamine hydrochloride) (PAH average M_w 50 000), docusate sodium salt (AOT), chloroform, and sodium chloride (NaCl) were received from Sigma-Aldrich, Poznan, Poland. Paclitaxel (PTX) was purchased from Selleck Chemicals, USA. Ultra-purified water was obtained using the Direct-Q 5UV purification system from Millipore. All chemicals were used without further purification.

2.2 Magnetically responsive PCL nanocarriers' preparation

Magnetically responsive polycaprolactone nanocarriers (MN-PCL NCs) were synthesized according to the procedure developed previously,[46] i.e., by Spontaneous Emulsification Solvent Evaporation (SESE) method, followed by the layer-by-layer (LbL) functionalization method. The synthesis is a two-step process, wherein the first step PCL nanocarriers (PCL NCs) are synthesized by the SESE method, while the second step consists of the encapsulation of synthesized PCL NCs into hybrid polyelectrolyte/SPIONs multilayer shells formed MN-PCL NCs. For the formation of drug-loaded PCL NCs, briefly, PCL, AOT, and Paclitaxel (PTX) were dissolved in chloroform. Such prepared oil phase was mixed with absolute alcohol and then gently added into a polycation aqueous solution under stirring.[46] After the stable nanoemulsion was formed, the organic solvent was evaporated by continuous stirring to finally formed the PTX-loaded PCL NCs. After the formation of PCL NCs, the polyelectrolyte/MN NPs multilayer shells were constructed by the saturation technique of the LbL method (the second step of MN-PCL NCs preparation). A fixed volume of PCL NCs was added to the oppositely charged polyelectrolyte's (PGA) solution, during vigorous mixing, and the consecutive layer formation was followed by the zeta potential measurements. Then, the coating process was repeated using the positively charged (zeta potential about +45 mV (ref. 46)) SPIONs. The procedure of sequential deposition of the polyelectrolyte's and SPIONs' layers was repeated until an appropriate number of layers in the hybrid multilayer shells was formed. As a result, the MN-PCL NCs were prepared. For safety issues, to perform hyperthermia and MRI experiments, blank nanocarriers (without paclitaxel) were prepared following the described procedure.

2.3 Magnetically responsive PCL nanocarriers' characterization

2.3.1 Average size, size distribution, and polydispersity. The average size (*i.e.* hydrodynamic diameter), size distribution, and polydispersity index (PdI) of all synthesized nanocarriers were carried out on a Zetasizer Nano ZS instrument (Malvern-Panalytical Ltd., UK) by Dynamic Light Scattering (DLS), with a He–Ne laser ($\lambda = 633$ nm, and scattering angle 173°). Each measurement was done in 0.015 M NaCl at 25 °C and each value was obtained as an average of three runs with at least 20 measurements.

DLS experiments on samples before and after the magnetic hyperthermia irradiation were performed with a Brookhaven 90Plus instrument (Brookhaven Instruments, USA) operating at ($\lambda = 658$ nm, and scattering angle 90°). Again, each measurement was done in 0.015 M NaCl at 25 °C.

2.3.2 Zeta potential measurements. The zeta potential of the nanocarriers was carried out on a Zetasizer Nano ZS instrument (Malvern-Panalytical Ltd., UK) by micro-electrophoretic mobility measurements, with a He–Ne laser ($\lambda = 633$ nm). Each measurement was done in 0.015 M NaCl at 25 °C as an average of at least three runs with 20 measurements.

2.3.3 Concentration measurements. The concentration of synthesized nanocarriers was assessed by the Nanoparticle Tracking Analysis (NTA) technique with the NanoSight NS500 instrument (Malvern-Panalytical Ltd., UK) equipped with a blue laser ($\lambda = 405$ nm). Each value was obtained in 0.015 M NaCl at 25 °C.

2.3.4 UV-Vis spectrophotometry. UV-Vis absorption spectra were acquired to confirm paclitaxel encapsulation into PCL nanocarriers by using a UV-1800 spectrophotometer (Shimadzu, Kyoto, Japan).

2.3.5 Stability of the nanocarriers. The stability of designed nanocarriers in 0.015 M NaCl was assessed by visual observation with time and at the storage temperature of 25 °C.

2.3.6 cryo-SEM, cryo-TEM and SEM-EDS observations. The morphology of obtained nanocarriers was determined by a cryo-SEM Jeol JSM 7600F FESEM (JEOL Ltd., Japan) according to the protocol described previously.[44]

cryo-TEM was used to characterize the structure MN-PCL NCs in suspension. The samples for cryo-TEM were prepared as described earlier.[47] A 3 μl drop of the sample was applied to an electron microscopy grid with carbon-covered polymer supporting film (lacey-carbon grids LC200-CuC, Electron Microscopy Sciences), glow discharged for 30 s with 5 mA current. Most of the sample was removed by blotting (Whatman No. 1 Filter paper) for 1 s, and the grid was immediately plunged into liquid ethane held at −183 °C. The sample was then transferred without rewarming into a Tecnai Sphera G20 electron microscope (FEI, Hillsboro, OR) using a Gatan 626 cryo-specimen holder (Gatan Inc., Pleasanton, CA). Images were recorded at 120 kV accelerating voltage and 11 500× microscope magnifications using a Gatan UltrScan 1000 slow scan CCD camera (giving a final pixel size from 2 to 0.7 nm). The applied underfocus typically ranged between 1.5 and 2.7 μm. The applied blotting conditions resulted in the specimen thickness varying between 100 and 300 nm.

SEM imaging before and after the magnetic hyperthermia irradiation were performed with a Field-Emission SUPRA40 Zeiss SEM equipped with a GEMINI FESEM detection column (Zeiss, Germany); in this case, a silicon wafer (area ~2 − 3 cm²) was cleaned and made highly hydrophilic by immersion in piranha solution (H_2SO_4 95% mixed with H_2O_2 36 volumes solution, ratio 3 : 1) for 1 hour and washed with ultrapure water. The substrate was immersed in a PAH polycation solution for 15 minutes, followed by 5 min immersion in water; finally, the substrate was immersed for 30 minutes in the MN-PCL NCs suspension, followed by 5 min immersion in water.

Energy Dispersive Spectroscopy (EDS) measurements were performed using a Silicon Drift Detector (SDD) X-act 10mm2 LN2-free (Oxford Instruments) mounted on the SUPRA40 Zeiss SEM microscope. Quantitative compositional analysis of EDS spectra was performed using the DTSA-II software[48] developed by NIST, which allows for detailed simulation of EDS emission spectra from bulk materials and nanostructures. EDS spectrum of MN-PCL NCs are averaged over 6 different nanocarriers; the spectrum of the substrate is averaged over 6 different regions with no adsorbed nanocarriers. Spectra were collected under irradiation with a 10 keV electron beam.

2.3.7 Magnetic resonance relaxometry and imaging. Two sets of agarose gel samples with varying concentrations of MN-PCL NCs were prepared to investigate contrasting properties and perform T_1 and T_2 relaxation measurements. Also, a reference sample containing non-diluted SPIONs – free nanoparticles were measured for comparison. In total, for each set, eight samples with different concentrations (0.015, 0.029, 0.058, 0.116, 0.232, 0.464, 0.929, 1.857 mmol L^{-1}) as well as a reference sample were investigated.

MR imaging as well as relaxometry were performed using the 9.4 T BioSpec 94/20 preclinical MRI scanner (Bruker BioSpin, Germany), equipped with BGA60-S gradient coils and 35 mm birdcage RF coil, controlled by Paravision 5.1 software. For the acquisition of the series of axial images of each sample, the RARE with variable repetition time TR (RAREVTR) imaging sequence was used. RAREVTR allows us to collect simultaneously data for T_1 and T_2 relaxation time maps of samples. To cover T_1 and T_2 relaxation curves, six TR (repetition time) values (5472, 2972, 1472, 772, 372 and 172 ms) and eight TE (echo time) values (3.7, 7.4, 11.1, 14.8, 18.5, 22.2, 25.9 and 29.6 ms) were used. Other imaging parameters were as follows: rare factor: 1, FOV: 40 × 40 mm, number of slices: 1, slice thickness: 4.0 mm, MTX size: 64 × 64.

Preliminary analysis of the mean signal intensities in the regions of interest *vs.* repetition (TR) or echo times (TE) were performed in Paravision 5.1, and further analysis was performed in MATLAB (MathWorks) and Origin 2020 (OriginLab).

T_1 and T_2 were determined *via* a single exponential curve fitting, except for T_2 measurement for the reference sample, where double-exponential behaviour was observed. For acquired T_1 and T_2 values, linear regression of the sample relaxation rates $\left(R_{1,2} = \dfrac{1}{T_{1,2}} \right)$ *vs.* SPIONs concentration

(proportional to nanocarriers concentration) in samples was performed:

$$R_{1,2} = R_{S1,S2} + r_{1,2 \times c}$$

where: c – concentration of SPIONs, $R_{1,2}$ – the measured sample relaxation rate, $R_{S1,S2}$ – the fitted relaxation rate of a solvent without MN-PCL NCs content, $r_{1,2}$ – the fitted relaxivity of nanocarriers with SPIONs.

2.3.8 Magnetic hyperthermia. The performance of MN-PCL NCs to heat their vicinity under the application of rf (radio-frequency) magnetic fields was tested by means of a DM100 nanoScale Biomagnetics apparatus for the measurement of magnetic hyperthermia. 1 mL batches of MN-PCL NCs suspension (1×10^{11} nanocarriers per mL) were irradiated using a 25 mT magnetic field oscillating at 429 kHz. The temperature of the sample was measured as a function of time with an optical fiber thermometer with a temperature sensitivity of ~0.1 °C.

3. Results and discussion

3.1 Synthesis and characterization of magnetically responsive polycaprolactone nanocarriers (MN-PCL NCs)

Magnetically responsive polycaprolactone nanocarriers (MN-PCL NCs) were synthesized by a two-step process schematically shown in Fig. 1. The first step consists of the formation of PCL nanocarriers (PCL NCs) by spontaneous emulsification solvent evaporation (SESE) method, while the second one consists of the formation of hybrid multilayer (polyelectrolyte/magnetic nanoparticles) shells by the layer-by-layer (LbL) method. In the first step, based on our previous experience,[46]

where optimized parameters for the preparation of polymeric nanocarriers were developed, the following oil phase consisting of PCL (10 mg mL^{-1}), AOT (330 mg L^{-1}), and Paclitaxel (PTX) was prepared by the dissolution of all components in an easily evaporative organic solvent (chloroform). Since the concentration of a drug has to be optimized for each system, the following range of concentration was tested: 0.9 to 15 mg mL^{-1}, according to the protocol described previously.[46] Such prepared oil phase was mixed with absolute ethanol (0.1 mL of the oil phase to 10 mL of the alcohol) and then gently added into 200 mL of an aqueous solution containing polycation (PLL, 200 ppm in 0.015 M NaCl) under stirring (500 rpm). That results in the formation of nanoemulsion stabilized by the AOT/PLL interfacial complex, which was used as a template for the PCL nanocarriers preparation by evaporation of an organic solvent *via* continuous stirring (24 hours). The final PCL NCs concentration assessed by NTA was approximately 1×10^{11} nanocarriers per mL, while the paclitaxel concentration in the final suspension was 3.75 mg L^{-1}. All details concerning the PCL NCs preparation are summarized in Table 2. An example of size distribution (measured by DLS), cryo-SEM image and UV-Vis absorption spectra are shown in Fig. S1 (ESI†).

As shown in Fig. S1a,† PCL nanocarriers with an average size of about 80 nm and a low polydispersity index (PDI < 0.15) could be obtained. It is also revealed that the average surface zeta potential of formed PCL NCs was +75 mV (±5 mV), which provides the capability of further functionalization by the LbL method. PTX encapsulation was confirmed by comparing UV-Vis spectra of PTX-loaded PCL NCs with empty ones (Fig. S1b†). The second step of magnetically responsive polycaprolactone nanocarriers' synthesis consists of the encapsulation of formed PCL nanocarriers in the hybrid multilayer
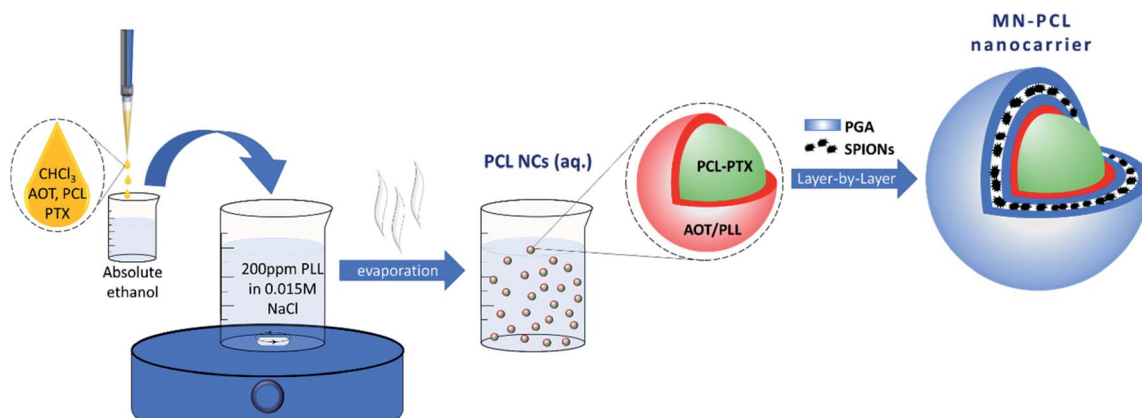

Fig. 1 Schematic representation of the synthesis of magnetically responsive polycaprolactone nanocarriers (MN-PCL NCs).

Table 2 The PCL nanocarriers' characterization

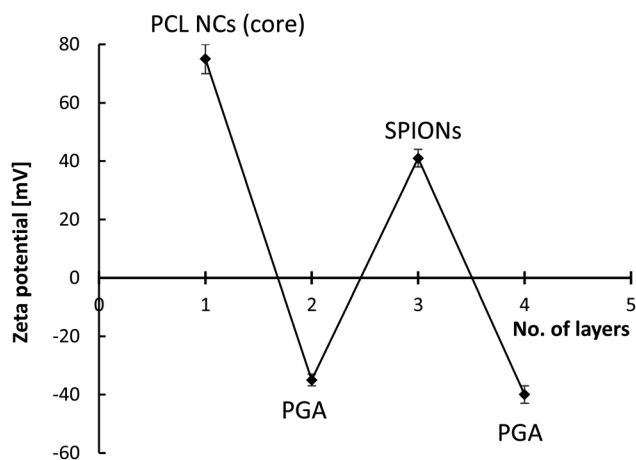| PCL : PTX concent.	Average size of PCL NCs	Polydispersity index (PDI)	Zeta potential of PCL NCs
5 mg L^{-1} : 3.75 mg L^{-1}	82 ± 6 nm	0.138 ± 0.011	+75 ± 5 mV

Fig. 2 Dependence of the PCL NCs' zeta potential on the adsorption of subsequent PGA/SPIONs layers.

(polyelectrolyte/magnetic nanoparticles) shells. The multilayer shells were constructed by the layer-by-layer adsorption of charged nano-objects technique with the saturation approach. In this technique, the rinsing steps are omitted since it is possible to add just enough charged nano-objects to completely coat all of the particles present in the system. Thus, little free unadsorbed nano-objects remain in the aqueous phase.[49] This is the most important advantage of the saturation technique since the classical LbL approach requires the rinsing step between adsorption of consecutive layers and that rinsing of nanocarriers is problematic and usually associated with their loss. The hybrid multilayer shell of PGA and SPIONs were formed on PCL nanocarriers. The saturation concentrations were determined empirically by monitoring changes of the zeta potential of PCL NCs during the formation of each layer at the nanocarrier's surface (Fig. S2a and b†). The saturation concentration of PGA, as well as SPIONs, corresponds to the point just before the plateau of the dependence of zeta potential
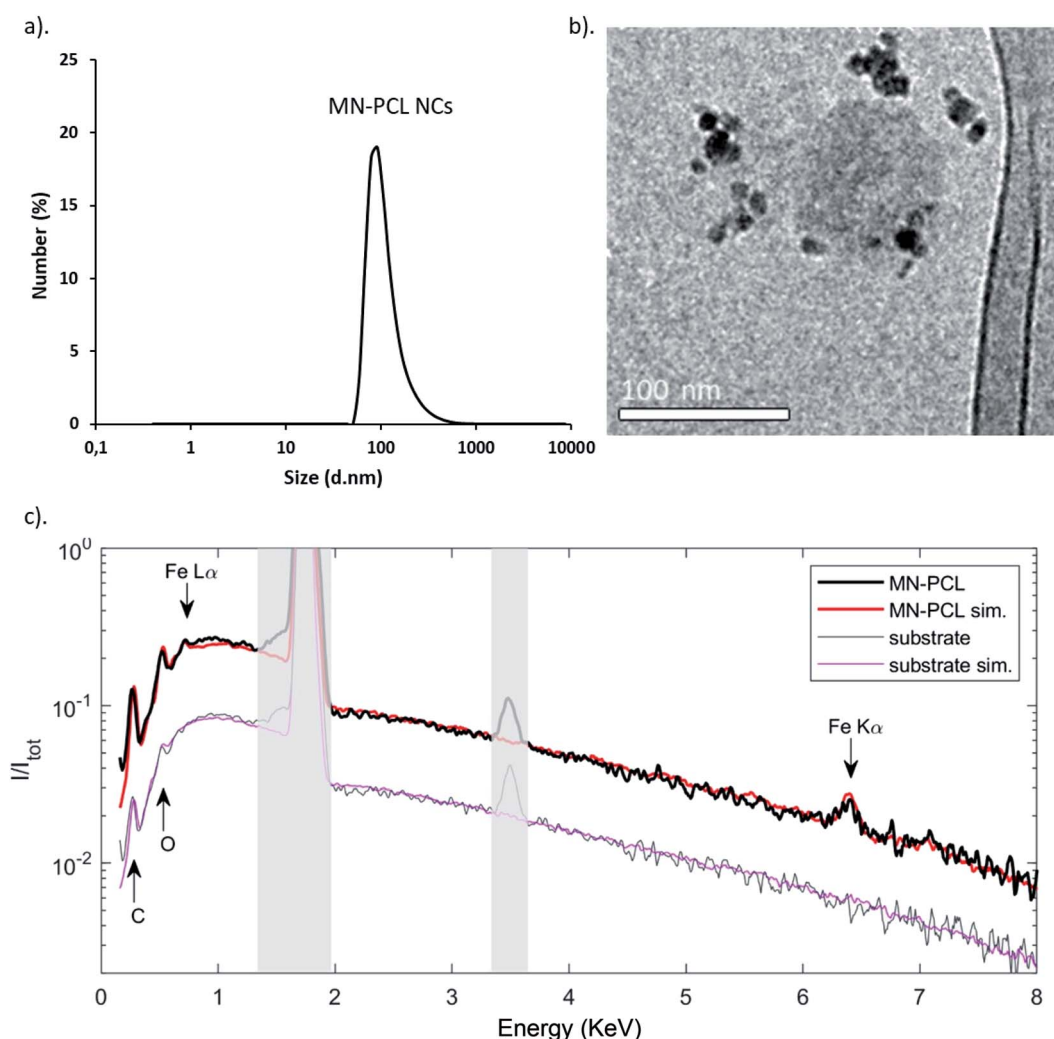

Fig. 3 Characterization of MN-PCL nanocarriers (a) size distribution measured by DLS, (b) cryo-TEM image (c) EDS spectrum of MN-PCL NCs (black) and of the substrate (gray), compared to simulations by NIST-DTSA2 software (red/magenta). Spectra are normalized; the regions marked in gray corresponds to the Si emission at 1.7 keV and to its pile-up artifact. Curves corresponding to MN-PCL NCs are scaled by a factor 3 to shift them and improve readability.

on the added amount of PGA or SPIONs is reached. The values are close to the zeta potential of PGA and SPIONs in solution or suspension, respectively.[46] Fig. 2 shows the typical saw-like dependence of the PCL NCs' zeta potential on the adsorption of PGA and SPIONs layers, which can be considered as the evidence of the successful formation of multilayer shells. The absolute values of zeta potentials of formed PCL-based nanocarriers, at each adsorption step, were higher than 30 mV which provided sufficient electrostatic stabilization against aggregation or agglomeration during the multilayer shells' formation.

Biomedical application of nanocarriers requires specific modification to eliminate recognition by the mononuclear phagocytic system and avoid fast clearance.[44,49] Polyethylene glycol (PEG) is widely used as a gold standard in bioconjugation and nanomedicine to prolong blood circulation time and improve drug efficacy; however, due to the immunogenicity issue of PEG, alternative strategies replacing PEG with other hydrophilic polymers, e.g., poly-amino acids like poly-L-glutamic acid (PGA) has been proposed.[49–52] Therefore, multilayer shells in our system were ended with PGA. It is worth noting that PEGylation is also possible according to our previous study.[46] The average size of the obtained hybrids, MN-PCL NCs was ~120 nm (PDI < 0.4) (Fig. 3a). The obtained values were in good agreement with the size of MN-PCL NCs visualized by the cryogenic Scanning Electron Microscopy (cryo-SEM) and Transmission Electron Microscopy (cryo-TEM); Fig. 3b. However, in the cryo-TEM image, we observe a partial decomposition of MN-PCL NCs.

The additional analysis of the EDS spectra (Fig. 3c) performed by the NIST-DTSA2 software allows the quantitative determination of the volume of the magnetic phase in the MN-PCL NCs. Initially, the EDS spectrum of the Si substrate (gray line) was simulated (magenta), accounting for the presence of SiO_2 and a PAH adhesion polymeric layer. The spectrum is naturally dominated by the Si emission peak at 1.74 keV, arising from the bulk of the substrate; besides this, C and O are also visible, at 0.28 and 0.54 keV respectively, together with an artifact at 3.48 keV which is due to pile-up and is related to the

Silicon Peak. As a next step, the spectrum measured on MN-PCL nanocarriers on the same substrate (black line) was simulated (red) by adding two additional layers, one formed by SPIONs and one by the PCL polymer. In this spectrum, new lines for Fe at 6.40 keV (Ka emission) and 0.70 keV (Lα emission) appear, and C and O lines grow in relative intensity. By modelling these layers, we obtain the indication that MN-PCL NCs are formed for $37 \pm 3\%$ by SPIONS and the remaining 63% by PCL.

The final MN-PCL NCs concentration assessed by NTA was approximately 1×10^{11} nanocarriers per mL, while the SPIONs concentration in the final MN-PCL NCs suspension was 0.92 mg mL^{-1}. Moreover, the hybrids were stable in-stock suspension for several weeks.

3.2 Magnetic drug delivery

Magnetic drug delivery is a targeted drug delivery approach that uses an external magnetic field to control the delivery of the drug to the specific site of action.[53–55] The magnetic field for drug targeting was firstly used in the 1950s while the first clinical trial was in 1996.[56–58] The research carried out on magnetic drug targeting can be summarized into two parts. The first one is the preparation of magnetic carriers, whereas the second one is the magnet design, i.e., a tool for the manipulation of magnetic carriers. An excellent book and comprehensive review of magnetic carriers[11] have been written.

Properties of developed MN-PCL NCs are optimized for biomedical application, namely the size, surface charge, and stability are favorable for passive targeting, where the target accumulation is based on enhanced permeability and retention (EPR) effect. Moreover, the incorporation of magnetic nanoparticles allows forming magnetically responsive nanocarriers that can accumulate at the desired site by an external magnetic field. One of the simple approaches simulating such a system is using a single permanent magnet, that is placed near the sample container. Due to the attractive force caused by the permanent magnet, the magnetically responsive carriers will be captured in the magnet area.[44,46,58] That approach was applied to
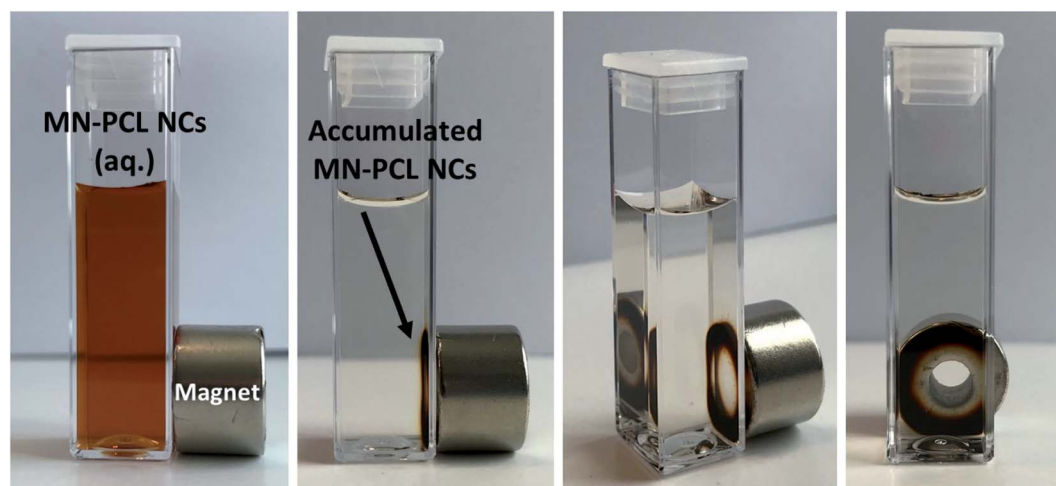

Fig. 4 Effect of the permanent magnet on synthesized MN-PCL NCs.

our MN-PCL NCs and is presented in Fig. 4. It can be clearly seen that our nanocarriers can be accumulated near the magnet. That simple experiment proved the concept of magnetic drug delivery, however, presented results are the simplest approach and more sophisticated experiments including various magnet systems should be performed.

3.3 Magnetic resonance relaxometry and imaging

Theranostics is defined as a material that combines the modalities of therapy and diagnostic imaging.[59,60] Thus, theranostics can simultaneously deliver therapeutic and diagnostic imaging agents within one entity. Encapsulation of a therapeutic agent, i.e., paclitaxel was presented above, therefore here we focused on diagnostic imaging. Among imaging modalities including optical imaging, MRI, computer tomography (CT), ultrasound (US), positron emission tomography (PET) or single-photon emission computed tomography (SPECT), each one possesses its unique advantages and limitations related to

sensitivity or spatial resolution.[61] Since SPIONs are promising contrast agents for MRI,[62,63] we tested our MN-PCL NCs as MRI detectable magnetically responsive nanocarriers.

An example of the MR images obtained at the shortest TE (i.e. 3.7 ms) for one set of the samples with different concentrations of nanocarriers (and thus SPIONs) is shown in Fig. 5. For the sample with the highest concentration ($n = 1.0 \times 10^{14}$ L^{-1} nanocarriers and $c = 1.86$ mmol L^{-1}) very rapid T_2 relaxation is observed, resulting in a signal intensity being very low even for this echo time. As the signal from further echoes was at the level of background noise it was not possible to fit T_2 relaxation time reliably for this concentration. Fig. 5a, also the image of the reference sample ($n = 1.0 \times 10^{14}$ L^{-1} nanocarriers and $c = 0$ mmol L^{-1}) with the highest signal, illustrates the significant contrasting effect of the presence of SPIONs.

Based on this data, relaxation time maps were calculated (Fig. 6), based on pixel-by-pixel fitting of exponential functions to the set of images measured for different TE and TR, showing significant dependence of relaxation times (especially T_2) on
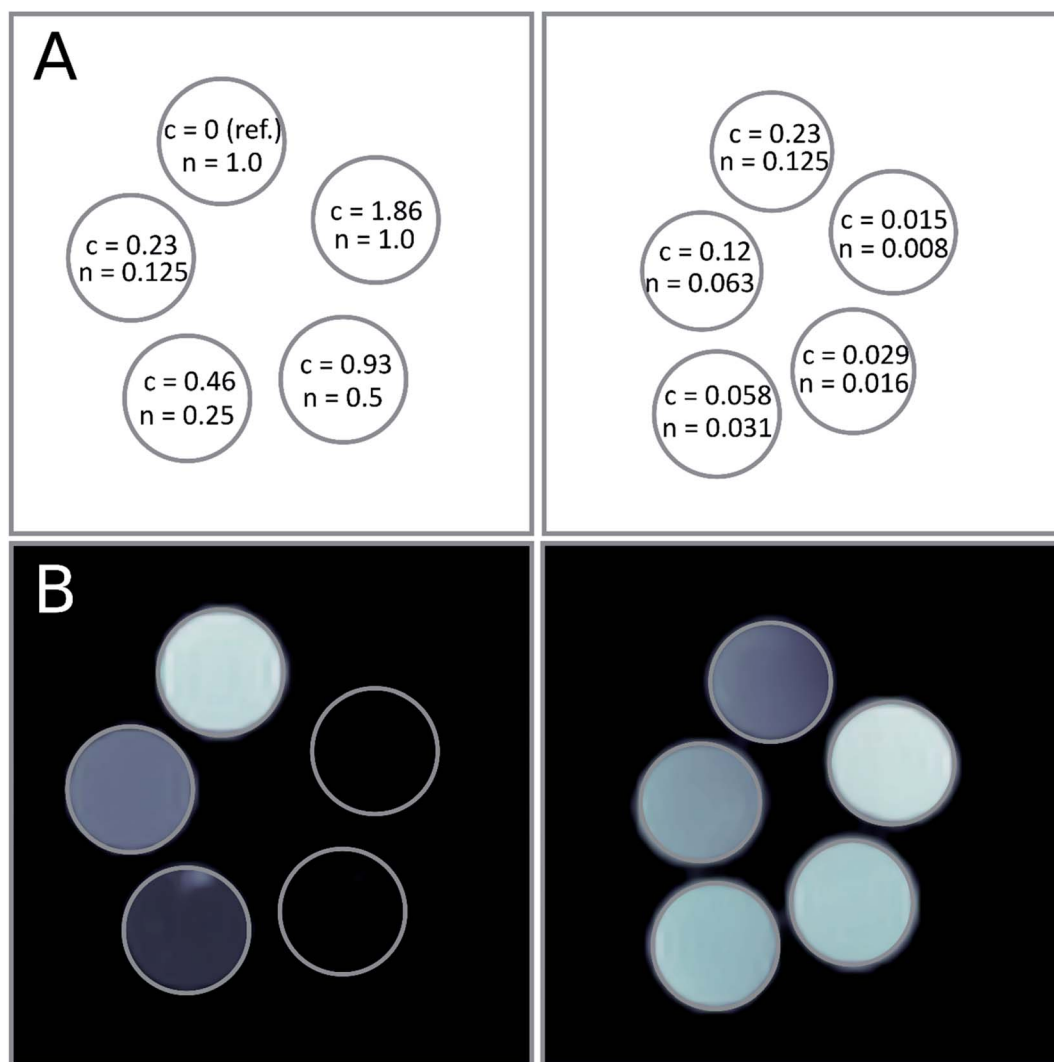

Fig. 5 (A) Arrangement of the samples in the scanner. (B) Axial images of samples containing different concentrations of SPIONs. RARE VTR sequence TE: 3.7 ms, TR: 5472 ms, n – number of nanocarriers [1.0×10^{14} L^{-1}], c – SPIONs concentration [mmol L^{-1}].
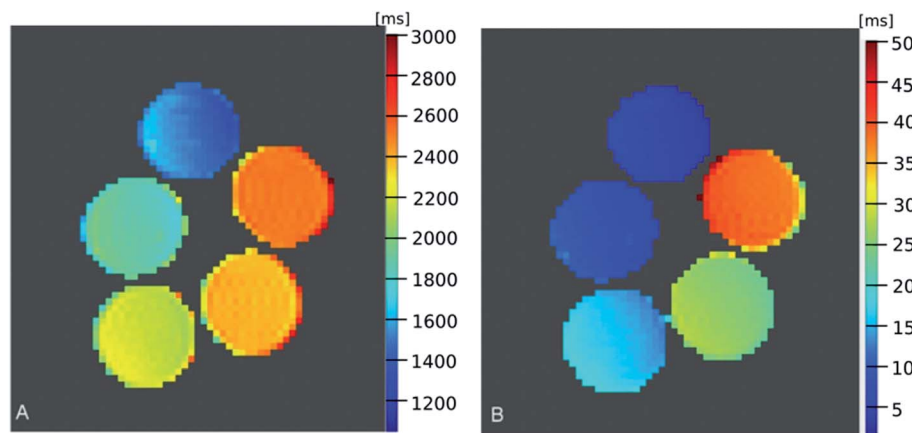
Fig. 6 T_1 (A) and T_2 (B) maps of the samples containing different concentrations of SPIONs (concentrations described in Fig. 5).

SPIONs concentration. As the pixel-by-pixel fitting for the high concentration of SPIONs were relatively unstable due to the fast decay of the signal with TE increase, only maps for lower concentration ranges are shown.

For better accuracy, fitting of the relaxation rates: R_1 and R_2 were accomplished based on ROI-averaged signals for both data sets. The dependences of the relaxation rates R_1 and R_2 vs. SPIONs concentration are presented in Fig. 7. The contrasting effect of SPIONs is significantly higher for R_2 than R_1, especially in a low concentration range, which is most interesting for potential clinical application, where minimizing the concentration, while maximizing required effects is expected. In a concentration range up to 0.23 mmol L^{-1}, a very good linear dependence of nanoparticles concentration on the R_2 relaxation rate (R_2 above 0.99) was observed. For higher concentrations, the T_2 shortening linearity is disturbed, which can be attributed to the clustering of NPs. For that reason, the specific relaxivity r_2 was determined only for unclustered NPs. The linear regression result for R_2 relaxation rate was: $R_2 = 10.67(\pm 0.38) + 850.1(\pm 10.1) \times c$. Results for R_1 showed linear dependence in the whole analyzed concentration range however the effect of T_1 shortening was much weaker. Linear regression results for R_1 relaxation rate was: $R_1 = 0.3509(\pm 0.0093) + 1.542(\pm 0.065) \times c$.

Obtained results showed that examined MN-PCL NCs exhibit a beneficial effect of modifying both R_1 and R_2 relaxation rates. In the chosen concentration range T_2 contrasting properties were much more profound, therefore proposed nanocarriers can serve as efficient "negative" contrast agents, which is greatly visible in T_2-weighted images (Fig. 5).

Even though many papers are presenting novel nanoparticles for use as multi-purpose theranostic devices, typically more attention is given to their therapeutic mechanisms than to the contrasting efficiency. Contrasting properties are examined mostly qualitatively[64] and values of relaxivities of synthesized nanoparticles are rarely presented. Moreover, contrasting properties of whole theranostic nanocarriers depend strongly not only on the characteristic of the used MRI contrasting component but mostly on its environment, which is directly affected by the composition of the whole nanocomposite. Reported relaxivities for multi-purpose nanocomposites with SPIONs are usually in the range of 120–250 mM Fe s^{-1}.[65,66] This range however gets much wider (up to a couple of hundred mM Fe s^{-1}) for simple SPIONs with different sizes and coatings.[67,68] For that reason, it is difficult to compare the contrasting efficiency of proposed nanoparticles with other results. Among several other metal oxides NPs, iron oxide demonstrates an
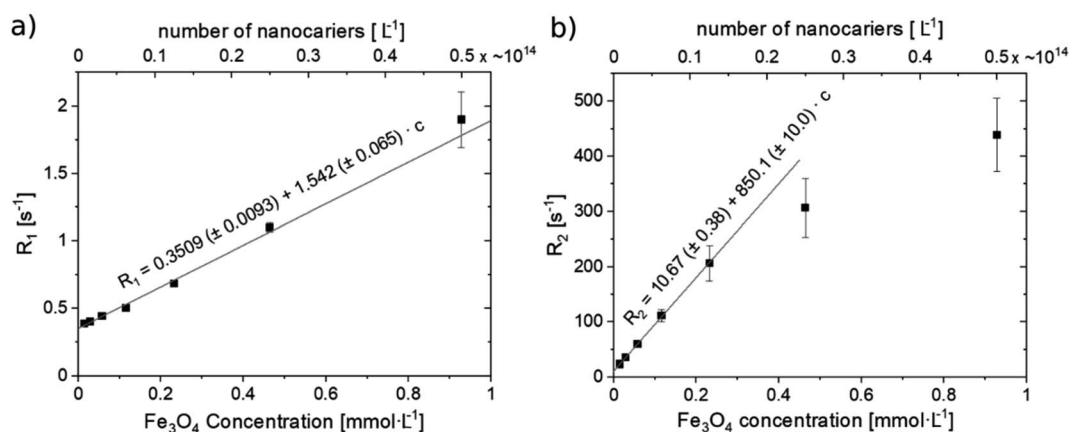

Fig. 7 Relaxation rate R_1 (a) and R_2 (b) of MN–PCL nanocarriers. Linear regression for R_1 fit weighted with T_1 uncertainties. Linear regression for R_2 weighted with T_2 uncertainties, in concentration range up to 0.23 mmol L^{-1}.

acceptable safety profile and non-cytotoxicity in concentrations <100 µg mL^{-1} (0.43 mM Fe$_3$O$_4$).[69] Uur experiment samples, with much smaller concentrations, were examined with satisfactory results; however, prediction of the appropriate dose of nanoparticles is impossible to make based on simple comparisons with other results. Although the very high transverse relaxivity result obtained for our nanoparticles is promising, other factors like nanocarriers intake and retention, heating rate (and resulting specific absorption rate), or drug (paclitaxel) dose have to be taken into consideration.

3.4 Magnetic hyperthermia

Hyperthermia is a heat treatment of organs or tissues that reduces the viability of cancerous cells, since the cells are more susceptible to temperature changes than normal cells.[70] The application of hyperthermia can be classified on its application strategy, distinguishing whole-body, regional, or local hyperthermia. Depending on the extent of local heat production, the temperature increase might have several effects on the cell:[71] (1) heating in the range 41–46 °C induces cell apoptosis triggered by a controlled alteration of structural and enzymatic functions of cell proteins; (2) heating above 46–48 °C (usually up to 56 °C) causes direct necrosis and coagulation. Moreover, tumor tissues possess a disorganized and compact vascular structure, their ability to dissipate heat is hindered. Therefore, hyperthermia causes a stronger response in tumor tissues than in healthy tissues.[72] Magnetic hyperthermia uses magnetic nanoparticles internalized in tumor cells to realize a localized heat generation. When SPIONs are irradiated with a radiofrequency (rf) alternating magnetic field, magnetic losses due to Néel and Brownian relaxations of their magnetization induce a localized temperature increase.

In this section, we report on the effects of a radiofrequency-oscillating magnetic field on a suspension of MN-PCL NCs, to investigate their performance as magnetic hyperthermia agents.

Fig. 8 reports on the irradiation of a 1 mL of MN-PCL NCs suspension (1×10^{11} nanocarriers per mL) with a 25 mT magnetic field oscillating at 429 kHz. The black curve is the temperature increase as a function of time. We fit the curve for the initial 90 seconds after the application of the magnetic field (red points) with a linear trend (red line), measuring the heating rate $\frac{\Delta T}{\Delta t}$; the Specific Absorption Rate (SAR) is then

$$\text{SAR} = \frac{cM}{m_{\text{Fe}_3\text{O}_4}} \frac{\Delta T}{\Delta t}$$

where c is the specific heat of water, M is the mass of water, and $m_{\text{Fe}_3\text{O}_4}$ is the mass of magnetic material. We found SAR = 55 ± 1 W g^{-1}.
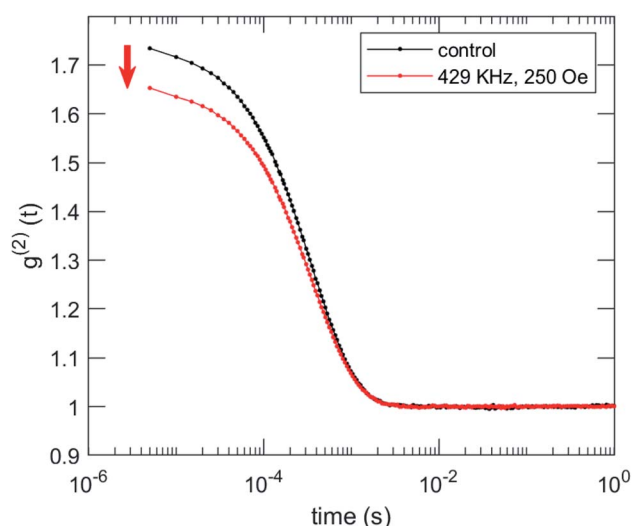

Fig. 9 DLS characterization of the effects of irradiation on MN-PCL NCs sample. Intensity correlation function g^2 (t) shows a loss of contrast after irradiation (red arrow).
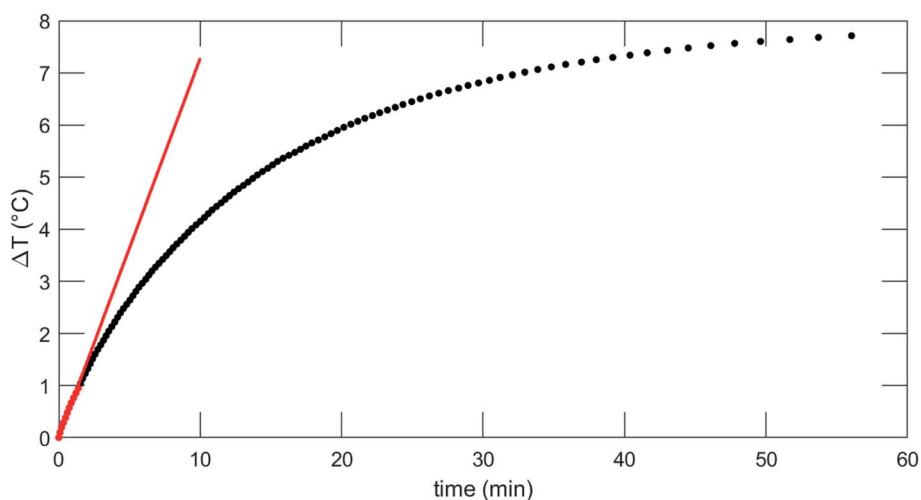

Fig. 8 Magnetic hyperthermia effect of MN-PCL NCs under irradiation with a 25 mT radiofrequency (f = 429 kHz) alternating magnetic field. The temperature increase ΔT with respect to ambient temperature is reported as a function of time (black points). The red line is a linear fit to the initial slope (time <90 s, red points), from which the specific absorption rate is determined.
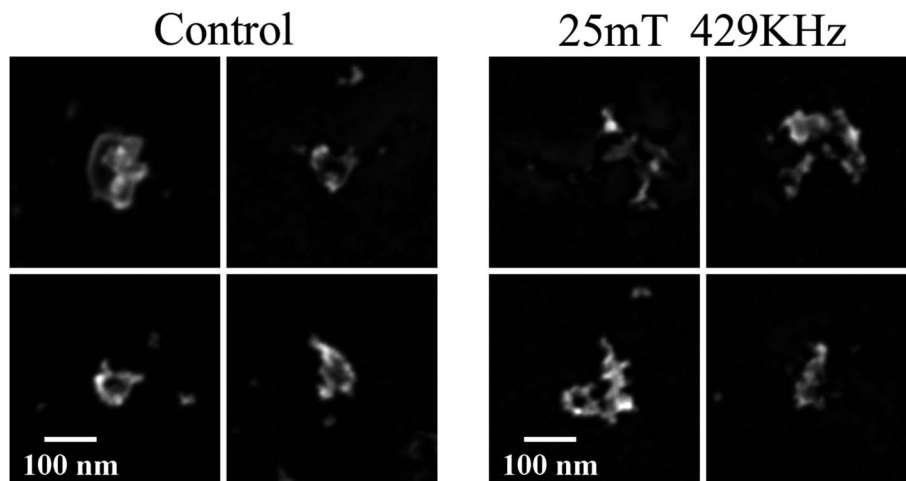
Fig. 10 SEM micrograph of MN–PCL NCs, before and after irradiation with rf magnetic fields. While the size of the objects is roughly unchanged, irradiated NCs have irregular shapes, indicating degradation.

We characterized the morphological effects of the hyperthermia treatment on the NCs by means of dynamic light scattering and scanning electron microscopy. DLS characterizations are reported in Fig. 9 for sample MN-PCL NCs. Both irradiated and control samples had the same count rate 43×10^3 cnt per s which is a good indication that the suspension is stable, against rf irradiation, excluding the occurrence of flocculation, sedimentation or creaming whatsoever. Visual inspection of correlation functions evidences an 11% loss of contrast upon rf irradiation, *i.e.*, a reduction of the value of $g^2(t)$ at the early times. This can be only attributed to the appearance of small debris, which induce decay of the correlation function in inaccessibly short times. Tentatively we identify these as objects with a hydrodynamic radius $R < 1$ nm, such as PGA molecules. An alternative explanation could also involve fast rotating anisotropic clusters. Notably, cumulant analysis[73] reported in Table S1 (ESI†) excludes major effects on overall size distribution of the MN-PCL.

SEM micrographs, reported in Fig. 10, confirm that irradiation with rf magnetic fields is altering the morphology of the NCs. Regularly shaped NCs are not found in the irradiated sample; on the contrary, we observe irregularly shaped objects and aggregates.

4.   Conclusion

A new type of multifunctional magnetically responsive polymeric-based nanocarriers was developed. The PCL nanocarriers were formed *via* the spontaneous emulsification solvent evaporation (SESE) method and further functionalized by the layer-by-layer (LbL) method. Model hydrophobic drug (paclitaxel) was encapsulated into the polymeric core, while SPIONs were incorporated into a multilayer shell. Properties of developed magnetically responsive polycaprolactone nanocarriers were optimized for biomedical applications, namely size (below 200 nm), low polydispersity index (PDI), surface modification (for prolonging blood circulation), and that can be monitored by MRI, and finally, that can locally increase temperature (local hyperthermia). The obtained results fulfill the first step of investigation for a biomedical application which is mandatory for the planning of any *in vitro* and *in vivo* studies. Further research will be focused on bioanalysis including biocompatibility, controlled release, and activity of the encapsulated drug, localization (MRI) as well as hyperthermia effect.

Conflicts of interest

The authors declare no conflict of interest.

Acknowledgements

References

1 S. Chen, *Polymer-coated iron oxide nanoparticles for medical imaging*, 2010.

2 C. Alexiou, R. J. Schmid, R. Jurgons, M. Kremer, G. Wanner, C. Bergemann, E. Huenges, T. Nawroth, W. Arnold and F. G. Parak, *Eur. Biophys. J.*, 2006, **35**, 446.

3 A. S. Arbab, L. A. Bashaw, B. R. Miller, E. K. Jordan, J. W. Bulte and J. A. Frank, *Transplantation*, 2003, **76**, 1123.

4 C. Corot, P. Robert, J. Idée and M. Port, *Adv. Drug Delivery Rev.*, 2006, **58**, 1471.

5 E. Y. Sun, R. Weissleder and L. Josephson, *Small*, 2006, **2**, 1144.

6 J. Wallyn, N. Anton and T. F. Vandamme, *Pharmaceutics*, 2019, **11**, 601.

7 A. K. Gupta and M. Gupta, *Biomaterials*, 2005, **26**, 3995.

8 C. Xu and S. Sun, *Adv. Drug Delivery Rev.*, 2013, **65**, 732.

9 A. A. A. Elrahman and F. R. Mansour, *J. Drug Delivery Sci. Technol.*, 2019, **52**, 702–712.

10 A. Lu, E. e. Salabas and F. Schüth, *Angew. Chem., Int. Ed.*, 2007, **46**, 1222.

11 U. Häfeli, W. Schütt, J. Teller and M. Zborowski, *Scientific and Clinical Applications of Magnetic Carriers*, Springer Science & Business Media, 2013.

12 Q. A. Pankhurst, J. Connolly, S. K. Jones and J. Dobson, *J. Phys. D: Appl. Phys.*, 2003, **36**, R167.

13 E. Denkhaus and K. Salnikow, *Crit. Rev. Oncol. Hematol.*, 2002, **42**, 35.

14 D. R. Haynes, T. N. Crotti and M. R. Haywood, *J. Biomed. Mater. Res.*, 2000, **49**, 167.

15 P. Reimer and R. Weissleder, *Radiologe*, 1996, **36**, 153.

16 A. S. Arbab, L. A. Bashaw, B. R. Miller, E. K. Jordan, B. K. Lewis, H. Kalish and J. A. Frank, *Radiology*, 2003, **229**, 838.

17 J. Chatterjee, Y. Haik and C. Chen, *J. Magn. Magn. Mater.*, 2003, **257**, 113.

18 R. Nisticò, F. Cesano and F. Garello, *Inorganics*, 2020, **8**, 6.

19 E. J. Bealer, K. Kavetsky, S. Dutko, S. Lofland and X. Hu, *Int. J. Mol. Sci.*, 2020, **21**, 186.

20 Y. Matsumura and K. Kataoka, *Cancer Sci.*, 2009, **100**, 572.

21 Y. Matsumura and H. Maeda, *Cancer Res.*, 1986, **46**, 6387.

22 S. Lu and J. Forcada, *J. Polym. Sci., Part A: Polym. Chem.*, 2006, **44**, 4187.

23 N. S. Barakat, *Nanomedicine*, 2009, **4**, 799.

24 U. Häfeli, *Int. J. Pharm.*, 2004, **277**, 19.

25 S. O. Aisida, P. A. Akpa, I. Ahmad, T. Zhao, M. Maaza and F. I. Ezema, *Eur. Polym. J.*, 2019, 109371.

26 S. Kurzhals, R. Zirbs and E. Reimhult, *ACS Appl. Mater. Interfaces*, 2015, **7**, 19342.

27 N. Nasongkla, E. Bey, J. Ren, H. Ai, C. Khemtong, J. S. Guthi, S. Chin, A. D. Sherry, D. A. Boothman and J. Gao, *Nano Lett.*, 2006, **6**, 2427.

28 R. Huang and Y. Zhang, *Bull. Chem. Soc. Jpn.*, 2018, **91**, 1697.

29 C. Vaccari, N. Cerize, P. Morais, M. I. Ré and A. Tedesco, *J. Nanosci. Nanotechnol.*, 2012, **12**, 5111.

30 S. German, N. Navolokin, N. Kuznetsova, V. Zuev, O. Inozemtseva, A. Anis'kov, E. Volkova, A. Bucharskaya, G. Maslyakova and R. Fakhrullin, *Colloids Surf., B*, 2015, **135**, 109.

31 O. Bixner and E. Reimhult, *J. Colloid Interface Sci.*, 2016, **466**, 62.

32 M. Martina, J. Fortin, C. Ménager, O. Clément, G. Barratt, C. Grabielle-Madelmont, F. Gazeau, V. Cabuil and S. Lesieur, *J. Am. Chem. Soc.*, 2005, **127**, 10676.

33 J. Odrobińska, E. Gumieniczek-Chłopek, M. Szuwarzyński, A. Radziszewska, S. Fiejdasz, T. Strączek, C. Kapusta and S. Zapotoczny, *ACS Appl. Mater. Interfaces*, 2019, **11**, 10905.

34 V. Torchilin, *Am. Pharm. Rev.*, 2013, **16**(5), https://www.americanpharmaceuticalreview.com/Featured-Articles/144241-Nanopreparations-for-Delivery-of-Non-Deliverable-Pharmaceuticals/.

35 C. Picart, F. Caruso and J. Voegel, *Layer-by-Layer Films for Biomedical Applications*, John Wiley & Sons, 2014.

36 G. B. Sukhorukov, E. Donath, H. Lichtenfeld, E. Knippel, M. Knippel, A. Budde and H. Möhwald, *Colloids Surf., A*, 1998, **137**, 253.

37 A. S. Angelatos, K. Katagiri and F. Caruso, *Soft Matter*, 2006, **2**, 18.

38 D. G. Shchukin and G. B. Sukhorukov, *Adv. Mater.*, 2004, **16**, 671.

39 K. Katagiri and F. Caruso, *Adv. Mater.*, 2005, **17**, 738.

40 A. S. Angelatos, K. Katagiri and F. Caruso, *Soft Matter*, 2006, **2**, 18.

41 D. G. Shchukin, I. L. Radtchenko and G. B. Sukhorukov, *J. Phys. Chem. B*, 2003, **107**, 86.

42 D. G. Shchukin, I. L. Radtchenko and G. B. Sukhorukov, *Mater. Lett.*, 2003, **57**, 1743.

43 F. Caruso, A. S. Susha, M. Giersig and H. Möhwald, *Adv. Mater.*, 1999, **11**, 950.

44 L. Cristofolini, K. Szczepanowicz, D. Orsi, T. Rimoldi, F. Albertini and P. Warszynski, *ACS Appl. Mater. Interfaces*, 2016, **8**, 25043.

45 K. Szczepanowicz, P. Piechota, W. P. Węglarz and P. Warszyński, *Colloids Surf., A*, 2017, **532**, 351.

46 M. Szczęch and K. Szczepanowicz, *Nanomaterials*, 2020, **10**, 496.

47 J. Dubochet, M. Adrian, J. Chang, J. Lepault and A. W. McDowall, in *Cryotechniques in Biological Electron Microscopy Anonymous*, Springer, 1987, p. 114.

48 D. E. Newbury and N. W. Ritchie, *J. Mater. Sci.*, 2015, **50**, 493.

49 K. Szczepanowicz, U. Bazylińska, J. Pietkiewicz, L. Szyk-Warszyńska, K. A. Wilk and P. Warszyński, *Adv. Colloid Interface Sci.*, 2015, **222**, 678.

50 A. Karabasz, K. Szczepanowicz, A. Cierniak, J. Bereta and M. Bzowska, *Int. J. Nanomed.*, 2018, **13**, 5159.

51 C. J. Hu, R. H. Fang, B. T. Luk and L. Zhang, *Nanoscale*, 2014, **6**, 65.

52 K. Szczepanowicz, H. Hoel, L. Szyk-Warszynska, E. Bielanska, A. Bouzga, G. Gaudernack, C. Simon and P. Warszynski, *Langmuir*, 2010, **26**, 12592.

53 V. P. Torchilin, *Nat. Rev. Drug Discovery*, 2014, **13**, 813.

54 B. Polyak and G. Friedman, *Expert Opin. Drug Delivery*, 2009, **6**, 53.

55 V. P. Torchilin, *Eur. J. Pharm. Sci.*, 2000, **11**, S81.

56 A. S. Lubbe, C. Bergemann, H. Riess, F. Schriever, P. Reichardt, K. Possinger, M. Matthias, B. Dorken, F. Herrmann, R. Gurtler, P. Hohenberger, N. Haas, R. Sohr, B. Sander, A. J. Lemke, D. Ohlendorf, W. Huhnt and D. Huhn, *Cancer Res.*, 1996, **56**, 4686.

57 R. K. Gilchrist, R. Medal, W. D. Shorey, R. C. Hanselman, J. C. Parrott and C. B. Taylor, *Ann. Surg.*, 1957, **146**, 596.

58 Y. Liu, D. Chen, P. Shang and D. Yin, *J. Controlled Release*, 2019, **302**, 90–104.

59 S. M. Janib, A. S. Moses and J. A. MacKay, *Adv. Drug Delivery Rev.*, 2010, **62**, 1052.

60 S. S. Kelkar and T. M. Reineke, *Bioconjugate Chem.*, 2011, **22**, 1879.

61 J. K. Willmann, N. Van Bruggen, L. M. Dinkelborg and S. S. Gambhir, *Nat. Rev. Drug Discovery*, 2008, **7**, 591.

62 C. Sun, J. S. Lee and M. Zhang, *Adv. Drug Delivery Rev.*, 2008, **60**, 1252.

63 S. Mornet, S. Vasseur, F. Grasset and E. Duguet, *J. Mater. Chem.*, 2004, **14**, 2161.

64 M. Liong, J. Lu, M. Kovochich, T. Xia, S. G. Ruehm, A. E. Nel, F. Tamanoi and J. I. Zink, *ACS Nano*, 2008, **2**, 889.

65 G. Yang, H. Gong, T. Liu, X. Sun, L. Cheng and Z. Liu, *Biomaterials*, 2015, **60**, 62.

66 J. Park, G. von Maltzahn, E. Ruoslahti, S. N. Bhatia and M. J. Sailor, *Angew. Chem.*, 2008, **120**, 7394.

67 F. Cheng, C. Su, Y. Yang, C. Yeh, C. Tsai, C. Wu, M. Wu and D. Shieh, *Biomaterials*, 2005, **26**, 729.

68 J. Huang, L. Bu, J. Xie, K. Chen, Z. Cheng, X. Li and X. Chen, *ACS Nano*, 2010, **4**, 7151.

69 S. Laurent, A. A. Saei, S. Behzadi, A. Panahifar and M. Mahmoudi, *Expert Opin. Drug Delivery*, 2014, **11**, 1449.

70 D. Joseph and M. Jose, *Res. J. Pharm. Technol.*, 2019, **12**, 1391.

71 D. Ruiz-Molina, F. Novio and C. Roscini, *Bio- and Bioinspired Nanomaterials*, John Wiley & Sons, 2014.

72 W. Dewey, L. Hopwood, S. Sapareto and L. Gerweck, *Radiology*, 1977, **123**, 463.

73 B. J. Berne and R. Pecora, *Dynamic Light Scattering: With Applications to Chemistry, Biology, and Physics*, Courier Corporation, 2000.